AD-A151 363 INTERMEDIATE RESULTS OF THE NORDSEE EXPERIMENT(U) 1/1
KANSAS UNIV/CENTER FOR RESEARCH INC LAWRENCE REMOTE
SENSING LAB R K MOORE ET AL. NOV 84 CRINC/RSL-TR-419-3
UNCLASSIFIED N00014-76-C-1105 F/G 17/9 NL

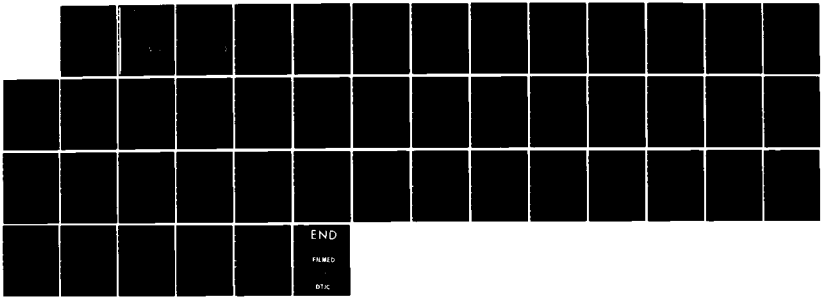

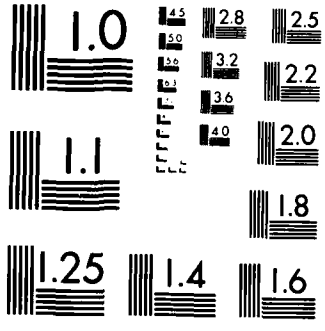

REMOTE SENSING LABORATORY

(3)

INTERMEDIATE RESULTS OF THE NORDSEE EXPERIMENT

THE UNIVERSITY of KANSAS CENTER for RESEARCH, INC.
2291 Irving Hill Drive-Campus West Lawrence, Kansas 66045

INTERMEDIATE RESULTS OF THE NORDSEE EXPERIMENT

R.K. Moore
V. Hesany
R. Lawner
S. Gogineni

Remote Sensing Laboratory
The University of Kansas
Center for Research, Inc.
Lawrence, Kansas 66045-2969

RSL Technical Report
RSL TR 419-3

November 1984

Supported by:

OFFICE OF NAVAL RESEARCH
Department of the Navy
800 N. Quincy Street
Arlington, Virginia 22217

CONTRACT N00014-76-C-1105

and

EUROPEAN SPACE AGENCY
Noordwijk, The Netherlands

CONTRACT 5706/83/NL/JS

TABLE OF CONTENTS

1.0 INTRODUCTION.....1

2.0 SYSTEM AND EXPERIMENT DESCRIPTION.....2

3.0 RESULTS.....3

3.1 Angular Responses.....4
3.2 Wind Speed.....4

4.0 SEA SPECTRUM.....15

4.1 Results.....15
4.2 Calculation of the Sea Spectrum, W(K).....15
4.3 Comparison with Previous Measurements and with Model.....21

5.0 MEASUREMENTS OF THE MODULATION TRANSFER FUNCTION.....22

5.1 Tilt Modulation.....24
5.2 Hydrodynamic Modulation.....27
5.3 Calculation of the MTF.....28
5.4 Preliminary Results.....29

6.0 CONCLUSIONS.....32

REFERENCES.....36

APPENDIX 1 Derivation of the Radar Signal Spectra.....37

LIST OF FIGURES

Figure 3.1: Angular Response of Scattering Coefficient at 5.3 GHz, Crosswind, VV-Pol.....5

Figure 3.2: Angular Response of Scattering Coefficient at U = 6.5 - 8.3 m/sec. Crosswind, VV-Pol, January 28, 1984.....6

Figure 3.3: Angular Response of Scattering Coefficient at 5.3 GHz, Upwind, VV-Pol, February 3, 1984. Aircraft Overflights.....7

Figure 3.4: Relationship between σ^0 and Wind Speed at 5.3 GHz.....9

Figure 3.5: Relationship between σ^0 and Wind Speed at 10 GHz.....10

Figure 3.6: Relationship between σ^0 and Wind Speed at 15 GHz.....11

Figure 3.7: Relationship between σ^0 and Wind Speed at 5.3 GHz.....12

Figure 3.8: Relationship between σ^0 and Wind Speed at 10 GHz.....13

Figure 3.9: Relationship between σ^0 and Wind Speed at 5.3 GHz.....14

Figure 3.10: Relationship between σ^0 and Wind Speed at 5.3 GHz.....16

Figure 4.1: Calculated Sea Spectrum for Upwind at Wind Speeds Ranging from 9-10 m/sec.....17

Figure 4.2: Calculated Sea Spectrum for Upwind at Wind Speeds Ranging from 12-13m/sec.....18

Figure 4.3: Calculated Sea Spectrum for Upwind at Wind Speeds Ranging from 15-18m/sec.....19

Figure 4.4: Calculated Sea Spectrum for Upwind at Wind Speeds Ranging from 20-22 m/sec.....20

Figure 5.1: A Linear System.....23

Figure 5.2: Spectra of Waveheight Calculated from Vertically Polarized 5.3 GHz Backscatter at a Pointing Angle of 55° and at a Wind Speed of 8.8 m/s in the Upwind Direction.....30

Figure 5.3: Sample Run for a Vertically Polarized 10 GHz Backscatter at a Pointing Angle of 64.8° and at a Wind Speed of 18.8 m/s in the Upwind Direction.....31

Figure 5.4: Sample Run for a Vertically Polarized 10 GHz Backscatter at a Pointing Angle of 64.8° and at a Wind Speed of 18.8 m/s in the Upwind Direction.....33

Figure 5.5: Sample Run for a Vertically Polarized 15 GHz Backscatter at a Pointing Angle of 55° and at a Wind Speed of 16.5 m/s in the Upwind Direction.....34

Figure 5.6: Sample Run for a Vertically Polarized 15 GHz Backscatter at a Pointing Angle of 55° and at a Wind Speed of 16.5 m/s in the Upwind Direction.....33

LIST OF TABLES

Table 1 System Specifications.....3
Table 2: Windspeed Exponents.....8
Table 3 Table of the Exponents.....15
Table 4 Ratios r_1 and r_2 at Different Slopes and Pointing Angles.....26

1.0 INTRODUCTION

Radar backscatter from the ocean has been the subject of considerable research since World War II. Most early studies aimed either at understanding the nature of sea "clutter" or determining the clutter statistics needed to optimize radar parameters necessary for detecting ships and other targets in the presence of clutter. These experimental programs indicated that radar return from the sea increased with wind speed, at least at low wind speeds, but at least one reported saturation at high wind speeds [Daley, 1973]. This, saturation, however, was shown by other investigators [e.g., Claassen, 1972] to be based on misreading of the experimental results.

During the mid-1960s, NASA Johnson Space Center initiated an experimental program to study the potential application of radars to oceanography. The results showed that a radar scatterometer can be used to measure winds over the ocean. Based on these results, Moore and Pierson [1971] advanced a proposal for measuring world-wide ocean winds with a spaceborne scatterometer.

Subsequent measurements conducted by NASA Langley Research Center under the Advanced Application Flight Experiments (AAFE) program further verified the dependence of scattering coefficient on wind speed. A major achievement of this program was the development by Jones et al. [1977] of circle-flight experiments that allowed more precise study of the directional dependence of scattering from the ocean.

During the same period SKYLAB was launched and many radar backscatter measurements were made with S-193 scatterometer from SKYLAB. These measurements further confirmed the usefulness of spaceborne scatterometry for oceanic wind studies.

SEASAT, the first satellite dedicated to remote sensing of oceans, was launched by NASA in June 1978. It carried a number of microwave remote sensors, one of which was a scatterometer designed for wind vector measurements. A large volume of data was collected during the three months of satellite operation, and analysis of this data confirmed that a spaceborne scatterometer can determine wind speed to the required accuracy.

The European Remote Sensing satellite (ERS-1) is scheduled to be launched during 1989. Instrumentation currently planned for ERS-1 includes an active microwave instrument at 5.3 GHz designed to function in three different

modes: (1) imaging, (2) wave, and (3) wind. The dependence of radar cross-section on wind speed at frequencies in C-band has not been investigated as extensively as that at higher frequencies in X- and Ku-bands. The European Space Agency initiated an experimental program during January - February 1984 to investigate the sensitivity of radar backscatter to windspeed at C-band. Tower-based radar backscatter measurements were made by The University of Kansas as a part of this experimental program.

The purpose of this report is to summarize the data collected during January 1984 from the Nordsee Tower in Germany. Brief descriptions of the system used and the experiment are given in Section 2.0. Angular responses of the scattering coefficient are discussed in Section 3.0. The apparent ripple spectra calculated from backscatter measurements are presented in Section 4.0, and the modulation transfer functions (MTFs) calculated from this data set are given in Section 5.0. Section 6.0 presents some general conclusions.

2.0 SYSTEM AND EXPERIMENT DESCRIPTION

A modified version of the University of Kansas helicopter-borne spectrometer (HELOSCAT) was used to acquire backscatter data during this experiment. The system measured radar scattering from the sea at frequencies from 4 to 17 GHz and incidence angles (relative to vertical) from 5° to 70°.

Internal (relative) calibration of the system was accomplished by measuring the signal from a delay line switched in place of the antenna before and after each data run. External (absolute) calibration was performed by measuring the power received from a target of known radar cross-section (a metal sphere with a diameter of 20 cm). Normally a Luneberg lens (which has a much higher cross-section than the metal sphere) is used for external calibration, but it was not possible to use the Luneberg lens during this experiment because of logistics problems. The important specifications of the system are given in Table 1. A more detailed description can be found in Gogineni et al. [1984].

The main emphasis of these measurements was on long data sets at a few fixed azimuth angles (generally upwind, downwind or crosswind) and incidence angles with VV-polarization at 5.3, 10 and 15 GHz. During aircraft

TABLE 1

SYSTEM SPECIFICATIONS

Type	FM-CW	
Frequency Range		4-17 GHz
FM Sweep	750 MHz	
Transmitted Power		5-16 dBm
Intermediate Frequency		50 kHz
IF Bandwidth	13.5 kHz	
Antenna:	Log-Periodic Reflector	
Polarization	VV, HH	
Size	61 cm	
Two-Way Effective Beamwidths	5.3, 10, and 15 GHz	5.2°, 2.8° and 2.0° at
Incident Angles		18° to 75° from vertical
Calibration:		
Internal	Delay Line	
External	Metal Sphere	
Height	24 meters	

overflights, measurements were made at 5.3 GHz at a fixed azimuth angle and the same incidence angle used by the systems in the aircraft.

In addition, the frequency response of ocean backscatter was measured by stepping the frequency at an interval of 400 MHz in C-band and 1 GHz between 9 and 17 GHz. Measurements at 5.3 GHz with VV-polarization at a fixed azimuth angle were also made when data with a cloverleaf buoy were being collected.

The experiment was conducted during January 21 - February 3, 1984. The windspeed varied from approximately 6 m/sec to 22 m/sec during this period.

3.0 RESULTS

Backscatter data from selected runs were used to compute the average scattering coefficient as a function of wind speed, direction and incidence angle.

3.1 Angular Response

The angular response of the scattering coefficient at 5.3 GHz for different wind speeds is shown in Figure 3.1. The backscatter increased by about 1 dB when the wind speed increased from approximately 7 m/sec to 13 m/sec at 18°. The radar cross-section difference between the two wind speed ranges increased with incidence angle between 18° and 40° and remained nearly constant at angles greater than 40°.

Backscatter from the ocean near vertical is believed to be dominated by large-scale roughness. It should, therefore, decrease with increasing wind speed. The increase in the scattering cross-section with wind speed between 18° and 70° indicates that Bragg scattering is the dominant mechanism for these angles of incidence.

Angular response of the scattering coefficient at 5.3, 10 and 15 GHz is shown in Figure 3.2. Backscatter data at 5.3 GHz were acquired during aircraft overflights, and data at 10 and 15 GHz were collected shortly after the overflights on January 28, 1984. At large incidence angles, the scattering coefficient at 10 GHz is about 3-4 dB higher than that at 5.3 GHz. The increase in the scattering cross-section is less than 2 dB between 10 and 15 GHz. The scattering coefficient increases gently with frequency.

The angular response of the scattering coefficient for the upwind direction at 5.3 GHz is shown in Figure 3.3. These measurements were made during aircraft overflights on February 3, 1984.

3.2 Wind Speed

One of the most widely used models to describe the dependence of radar backscatter on wind speed is the power-law relationship and is given by:

$$\sigma^{o}(\theta) = a(\theta)\, u^{\gamma(\theta)}$$

where:

$a(\theta)$ = leveling coefficient

$\gamma(\theta)$ = wind speed exponent

u = wind speed in m/sec.

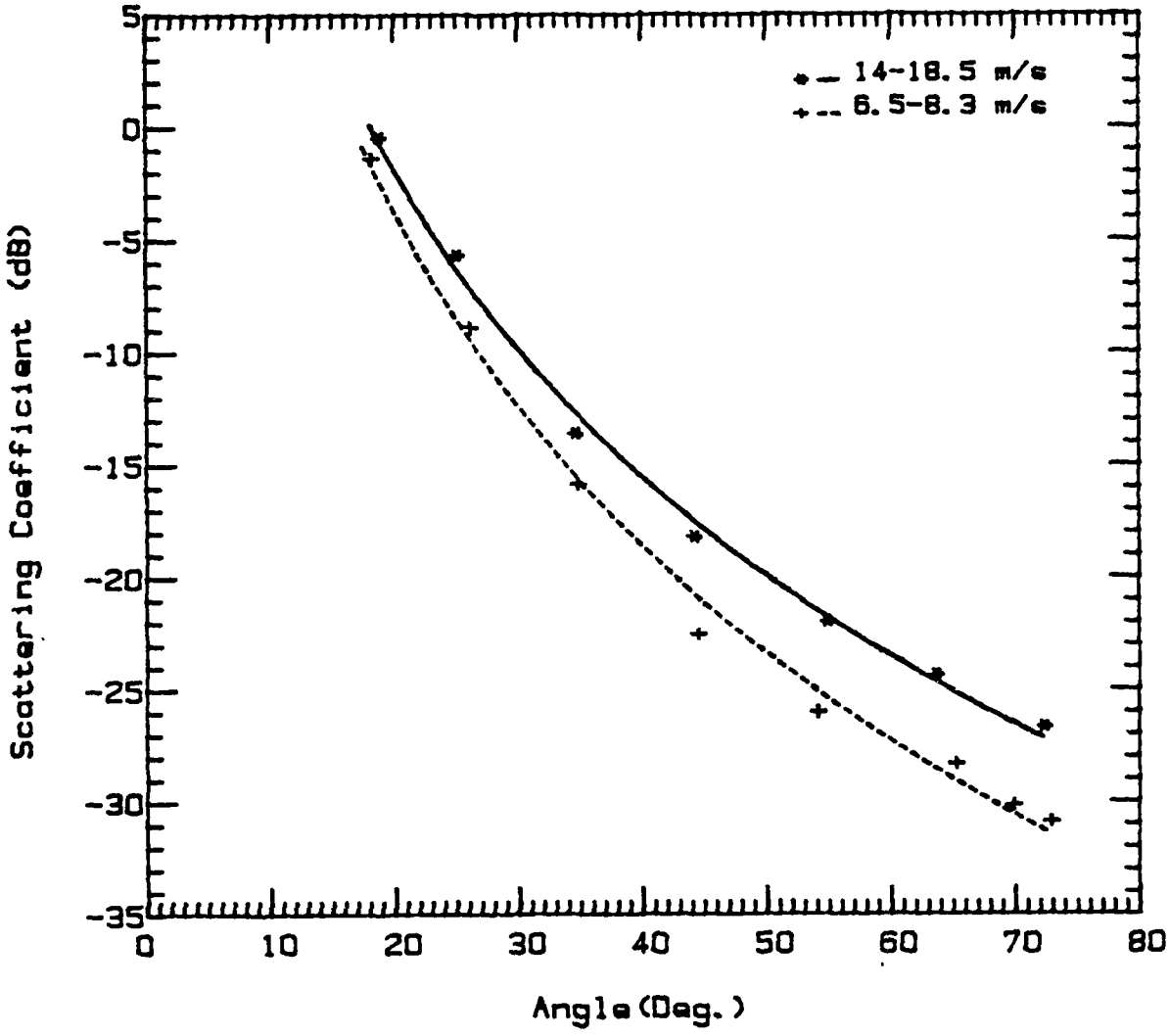

FIGURE 3.1: Angular Response of Scattering Coefficient at 5.3 GHz. Crosswind, VV-Pol.

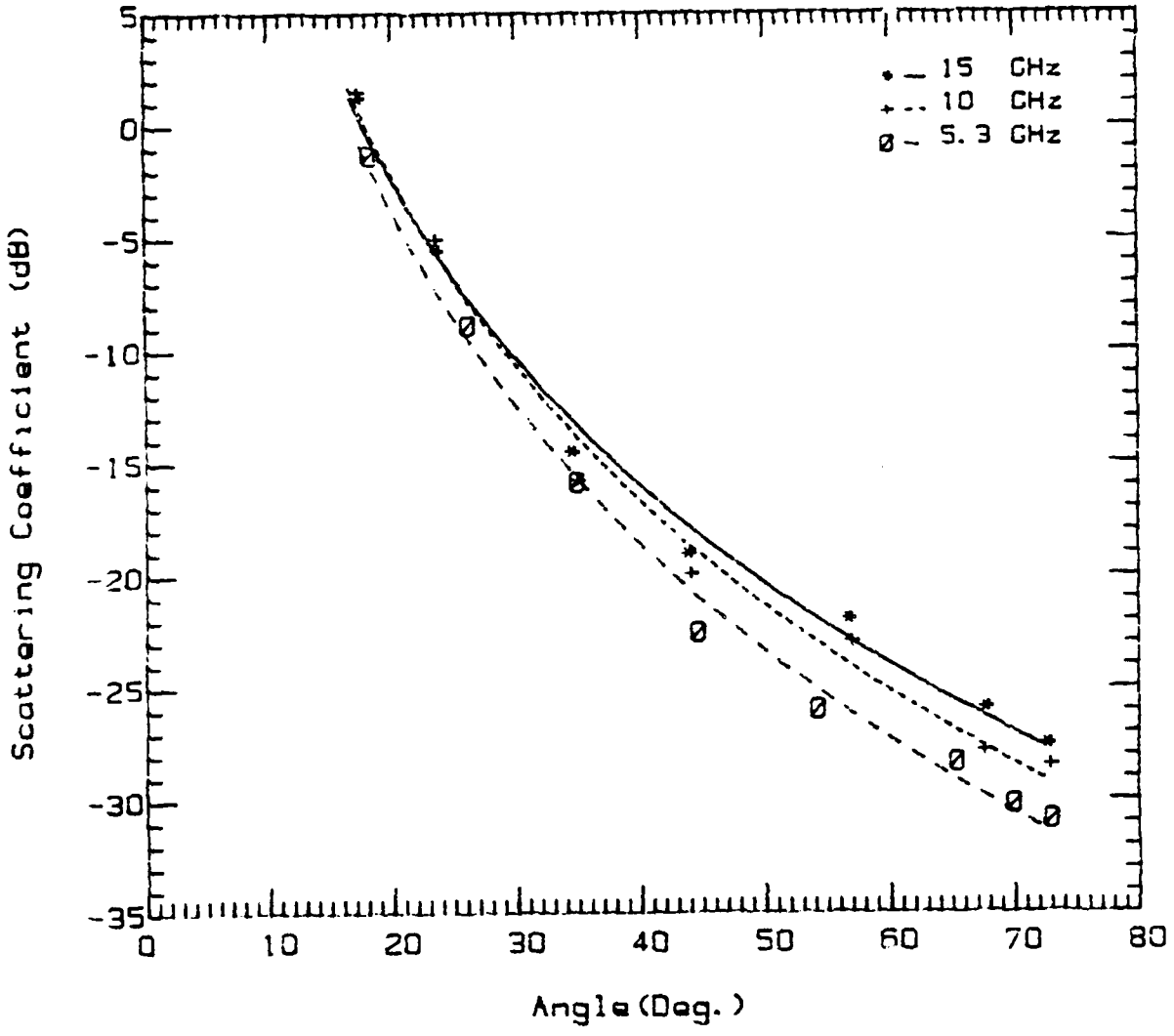

FIGURE 3.2: Angular Response of Scattering Coefficient at U = 6.5 - 8.3 m/sec. Crosswind, VV-Pol., January 28, 1984.

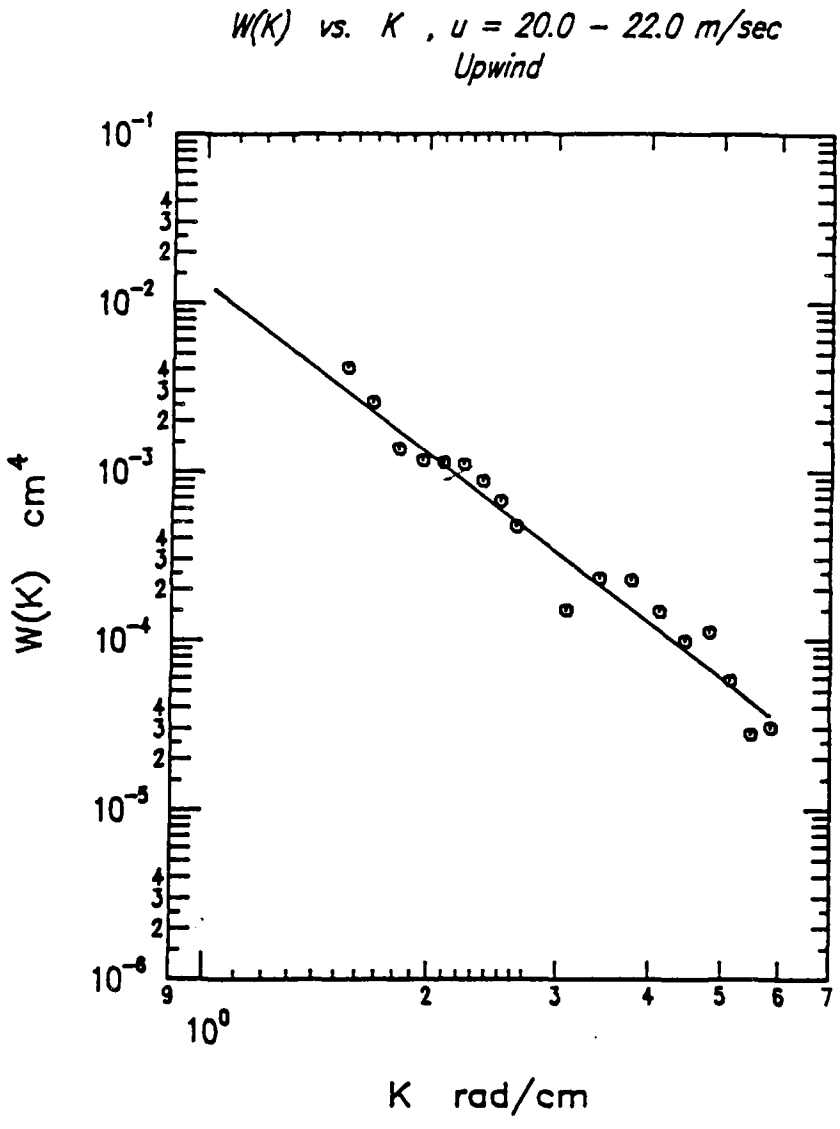

FIGURE 4.4: Calculated Sea Spectrum for Upwind at Windspeeds Ranging from 20 to 22 m/sec

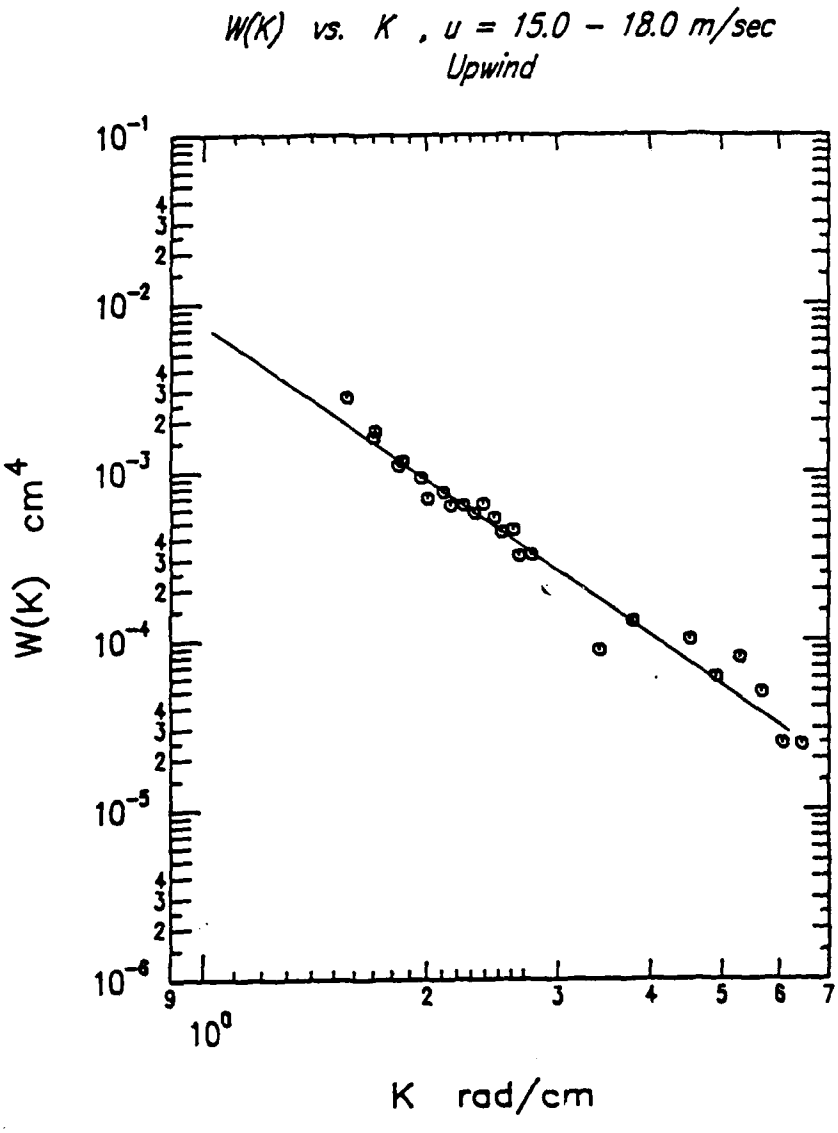

FIGURE 4.3: Calculated Sea Spectrum for Upwind at Wind Speeds Ranging from 15 to 18 m/sec.

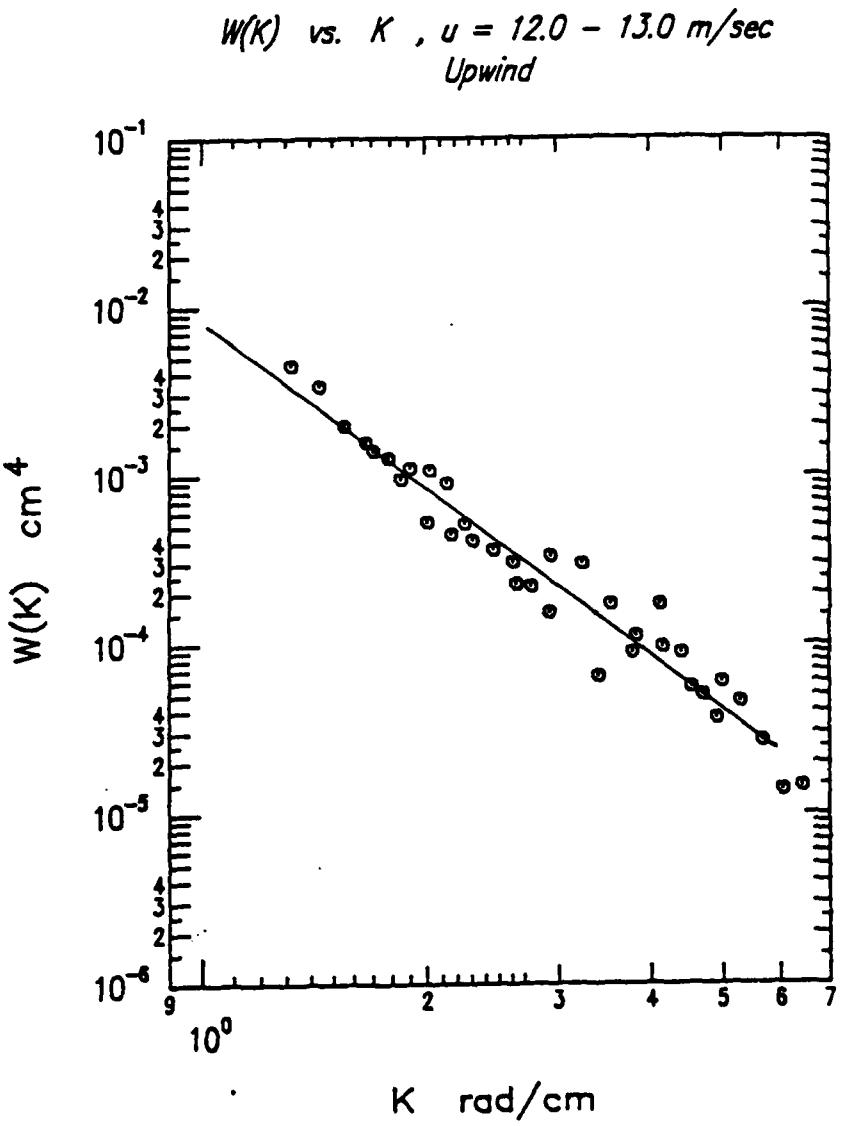

FIGURE 4.2: Calculated Sea Spectrum for Upwind at Wind Speeds Ranging from 12-13 m/sec.

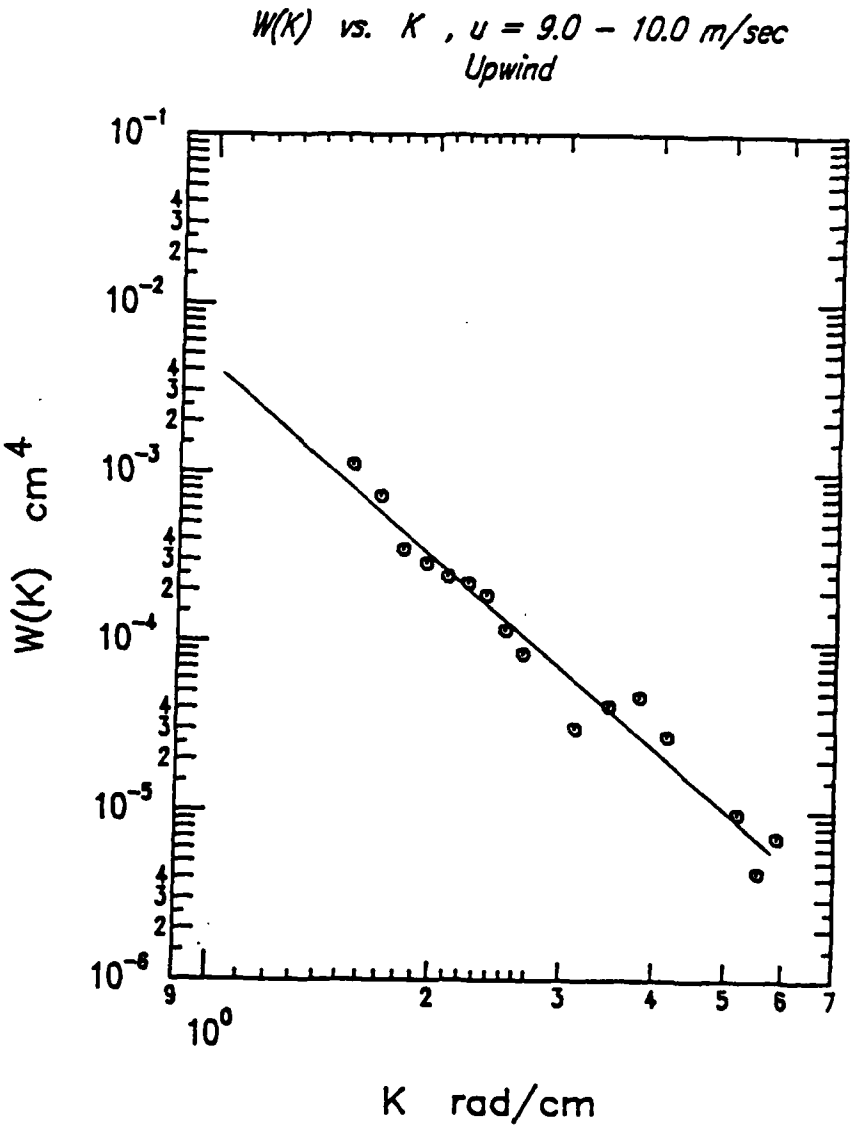

FIGURE 4.1: Calculated Sea Spectrum for Upwind at Wind Speeds Ranging from 9 to 10 m/sec.

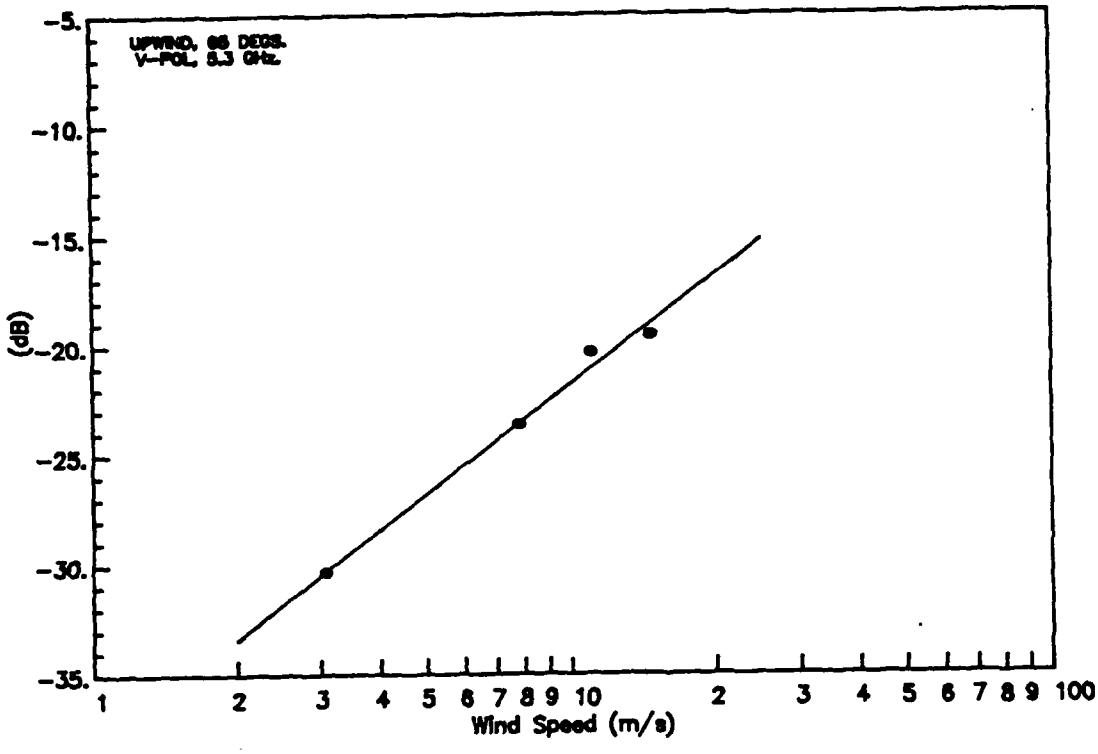

FIGURE 3.10: Relationship Between σ^0 and Wind Speed at 5.3 GHz

Scattering coefficient vs windspeed for the upwind direction at 5.3 GHz and incidence angle of 65° is shown in Figure 3.10. The exponent at 65° is lower than that at 55°.

4.0 SEA SPECTRUM

4.1 Results

Selected radar backscattering measurements at frequencies ranging from 4.5 - 17 GHz, and incidence angles ranging from 45° to 65°, were used to calculate apparent ripple spectra at various windspeeds. Only VV polarization was used for these measurements, all of which were in the upwind direction. The results are shown in Figures 4.1 - 4.4. In each of these figures the line shown is a regression fit of the form

$$W(K) = AK^{-\alpha}$$

for the points shown. The exponent α is tabulated in Table 3, which also includes values of the coefficient A.

TABLE 3

TABLE OF THE EXPONENTS

Windspeed m/s	α	A
9 - 10	3.73	4.07×10^{-3}
12 - 13	3.30	8.32×10^{-3}
15 - 18	3.03	7.41×10^{-3}
20 - 22	3.37	1.380×10^{-2}

4.2 Calculation of the Sea Spectrum, W(K)

The calculation of sea spectrum values was made using the small perturbation theory [Fung and Lee, 1982; Fung and Chan, 1977; Lawner and Moore, 1985]. According to this, the backscattering coefficient for vertical polarization is given by

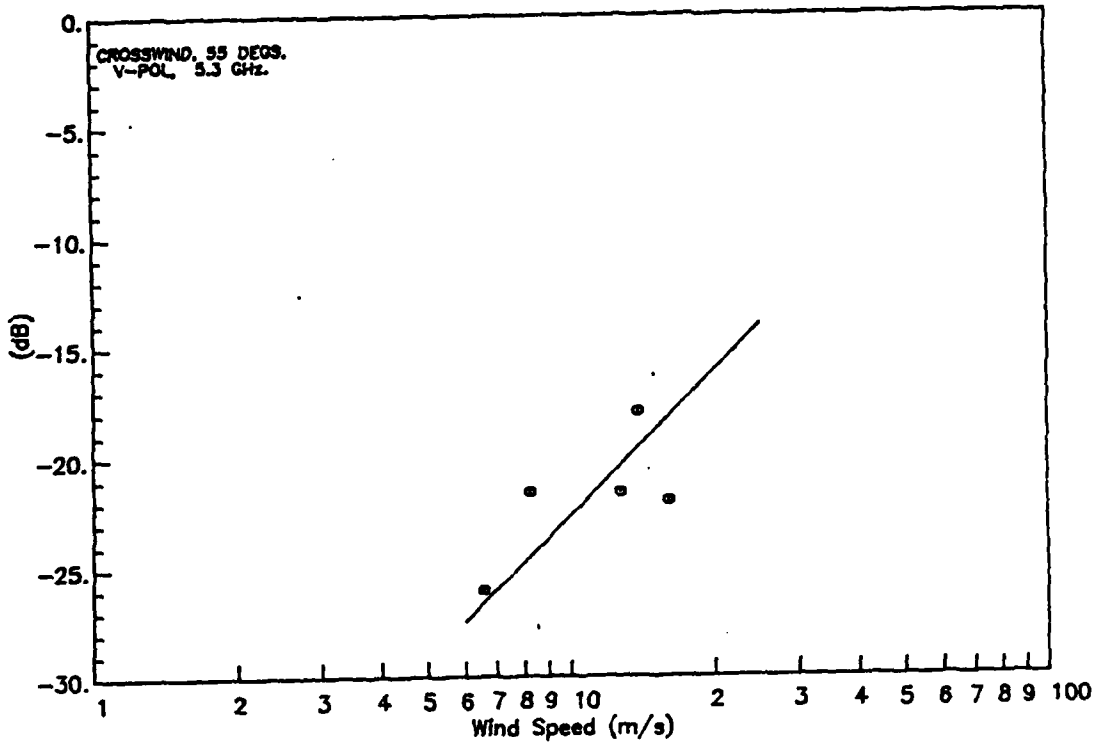

FIGURE 3.9: Relationship Between σ^0 and Wind Speed at 5.3 GHz

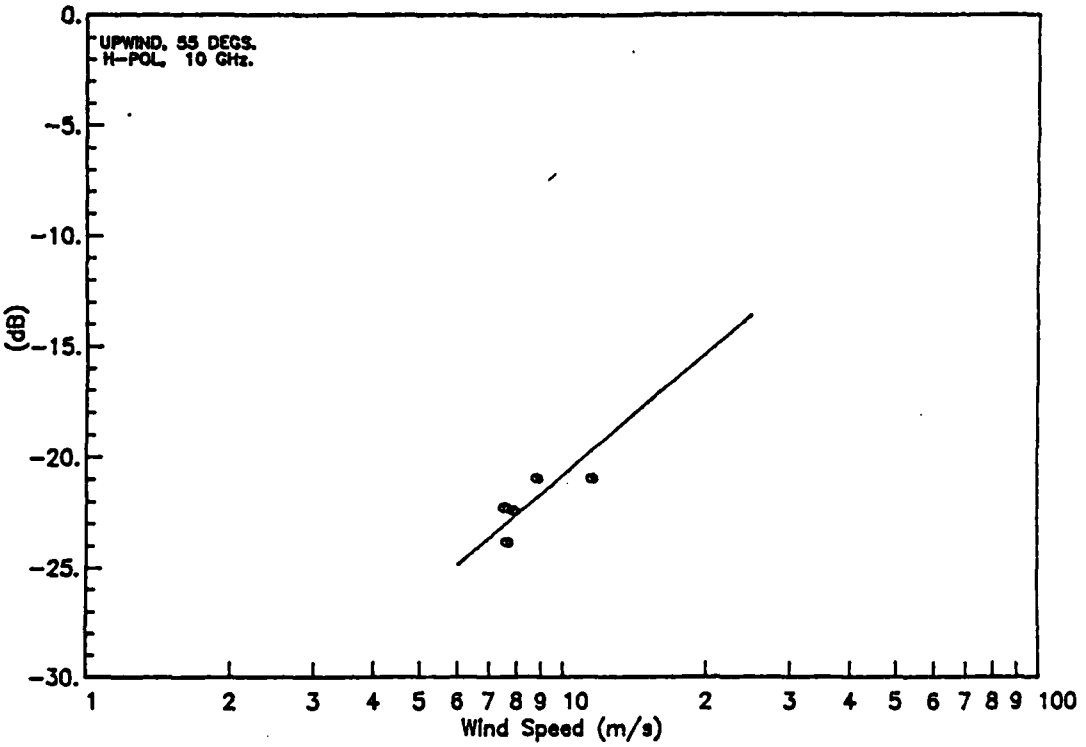

FIGURE 3.8: Relationship Between σ^0 and Wind Speed at 10 GHz

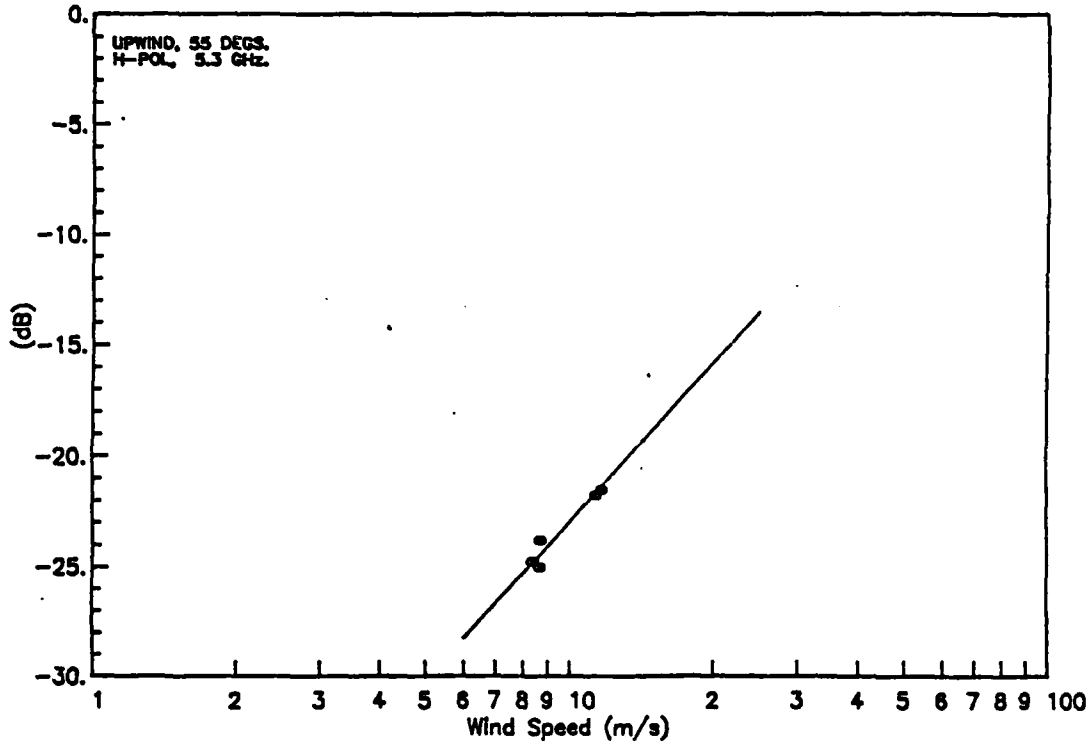

FIGURE 3.7: Relationship Between σ^0 and Wind Speed at 5.3 GHz

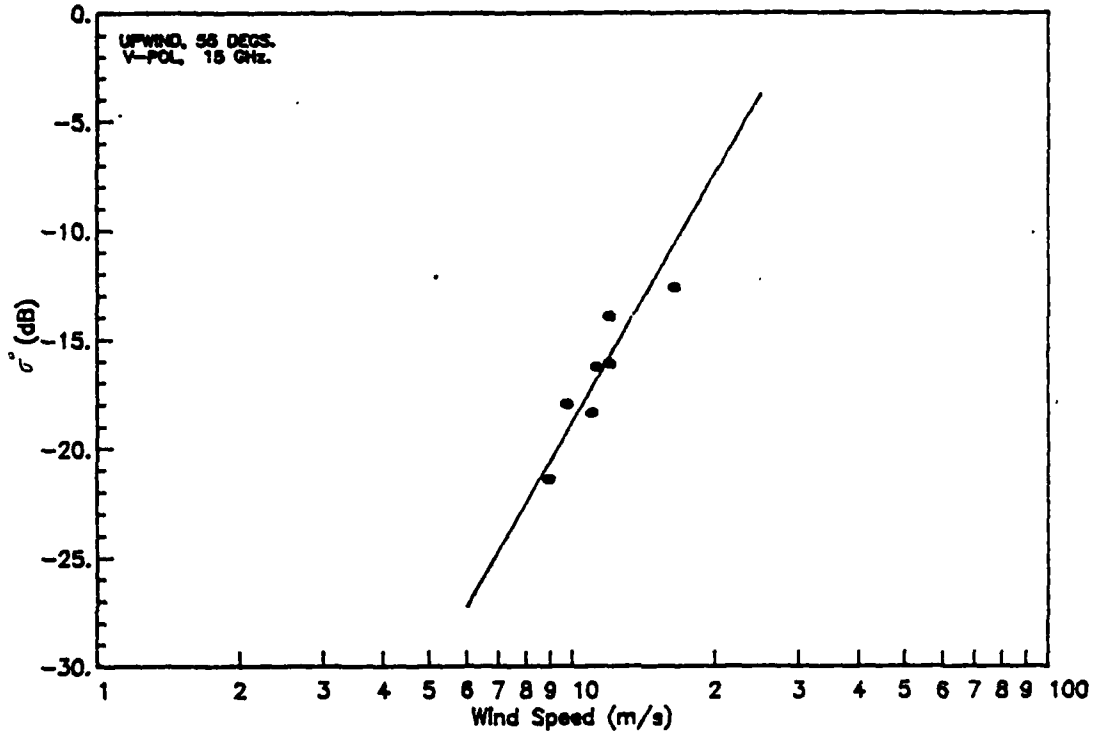

FIGURE 3.6: Relationship Between σ^0 and Wind Speed at 15 GHz

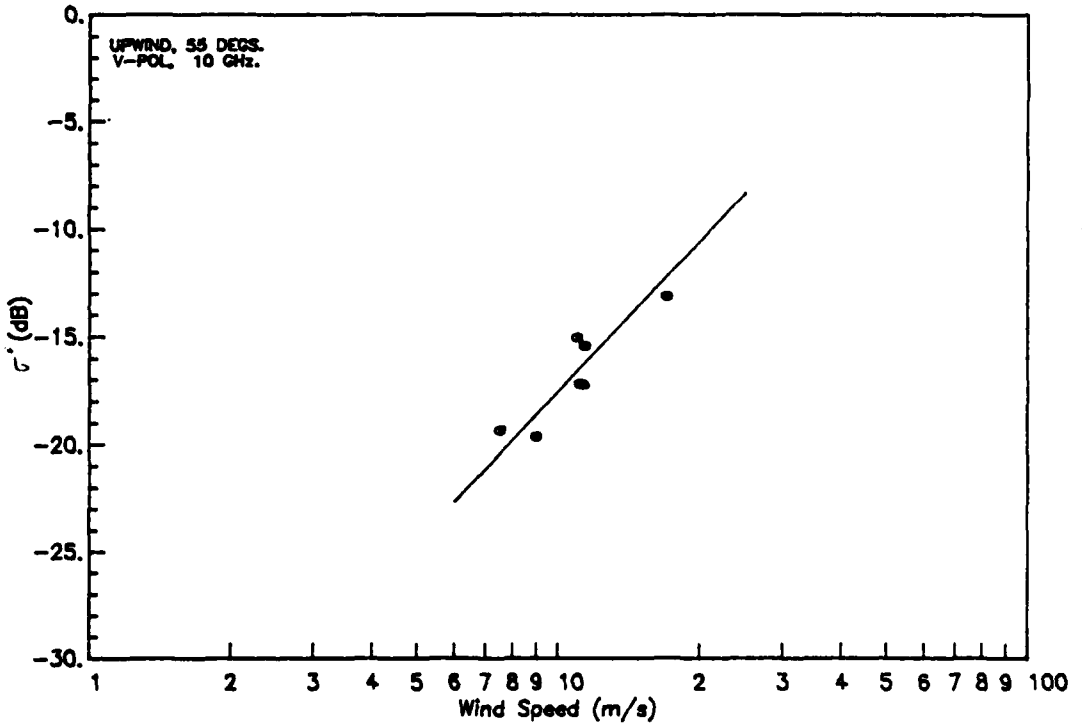

FIGURE 3.5: Relationship Between σ^0 and Wind Speed at 10 GHz

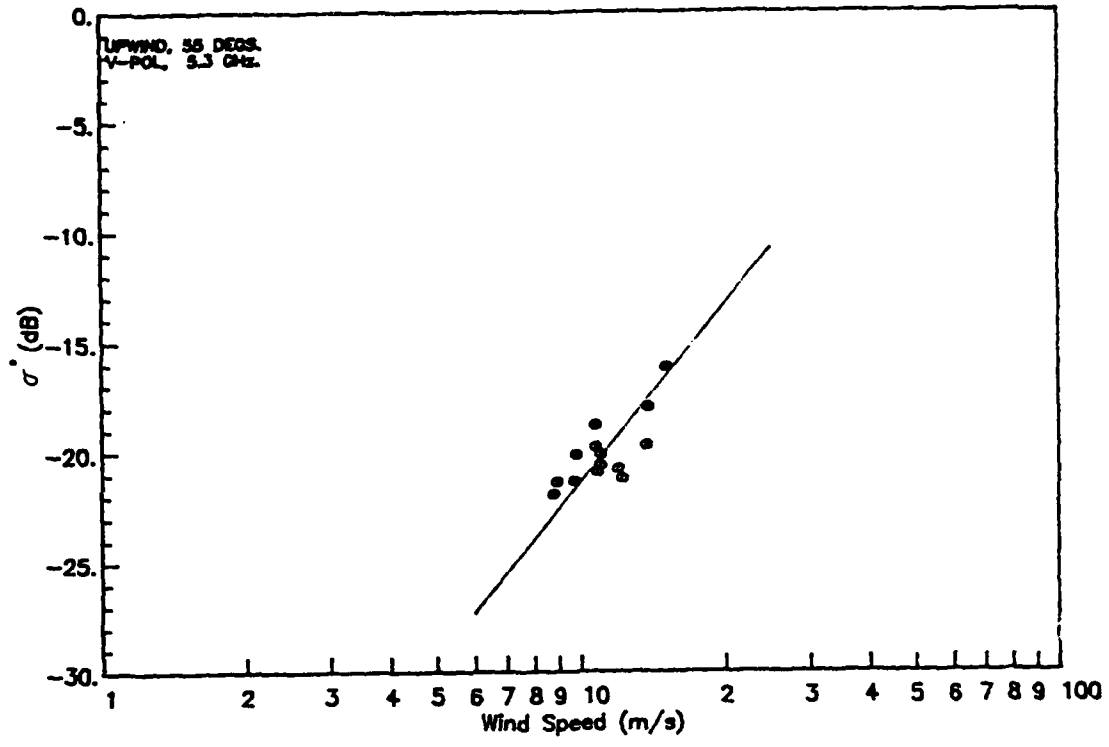

FIGURE 3.4: Relationship Between σ^0 and Wind Speed at 5.3 GHz

The relationship is generally expressed in log-log form as:

$$\sigma^{o}(dB) = A + B \log(u)$$

where:

$$A = 10 \log (a(\theta))$$

$$B = 10\gamma$$

Scattering coefficient as a function of wind speed for upwind direction at 5.3, 10 and 15 GHz is shown in Figures 3.4 - 3.6 for **VV polarization.** The sensitivity to wind speed is higher at 15 GHz, but the scattering coefficient at 5.3 GHz also increases with wind speed. The exponent at 15 GHz is much higher than those at 5.3 and 10 GHz. It is also much higher than that reported during earlier investigations. Each new experiment seems to produce exponents slightly higher than those during the previous experiments! Possible causes could be either an inaccurate calibration or a loss of precision in estimating the scattering coefficient at higher frequencies because of lower signal-to-noise ratio (at lower wind speeds), but the effect may also be real.

The wind speed response at 5.3 and 10 GHz for the upwind direction with **HH-polarization** is shown in Figures 3.7 and 3.8, respectively. The sensitivity to wind speed at 5.3 GHz is higher than that at 10 GHz. The data reported in these figures were collected during different times. The scatter in the data points at 10 GHz might be because of a change of environmental parameters.

Wind speed response at 5.3 GHz for the crosswind direction is shown in Figure 3.9. The exponent (2.15) for crosswind direction is lower than that for upwind (2.67) direction. (See Table 2).

TABLE 2

WINDSPEED EXPONENTS

Figure	Freq. (GHz)	Pol.	Wind Dir.	Inc. Angle (°)	$10^4 a$	γ
3.4	5.3	VV	upwind	55	.156	2.67
3.5	10 VV	upwind	55	.234	2.31	
3.6	15 VV	upwind	55	.021	3.79	
3.7	5.3	HH	upwind	55	.215	2.37
3.8	10 HH	upwind	55	1.271	1.81	
3.9	5.3	VV	crosswind	55	.386	2.15

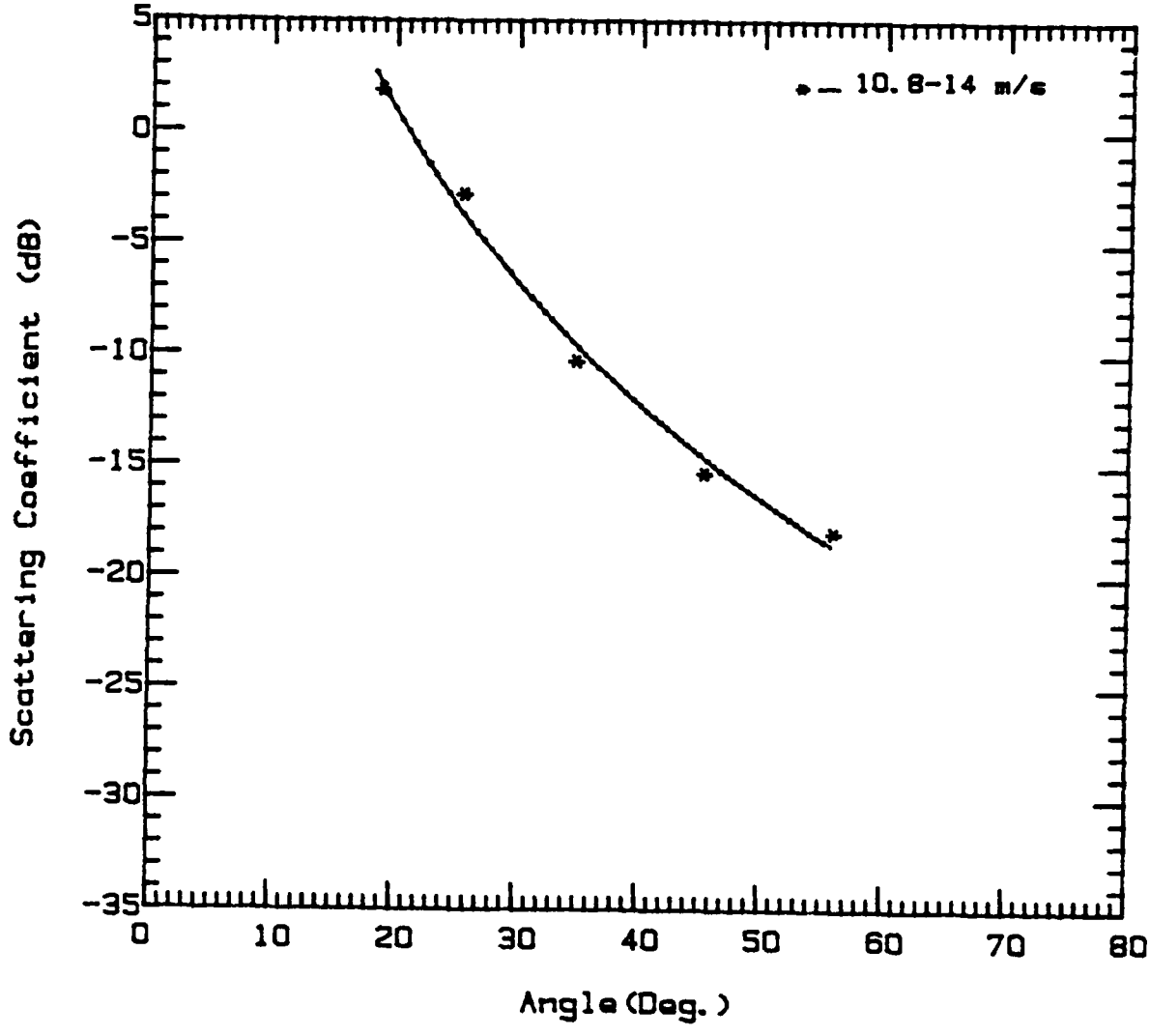

FIGURE 3.3: Angular Response of Scattering Coefficient at 5.3 GHz. Upwind, VV-Pol., February 3, 1984. Aircraft Overflights.

$$\sigma_{VV}(k,\phi) = 8k^4|\alpha_{VV}|^2\, S(K,\phi)/K \qquad (4.1)$$

where K is the ocean-surface wavenumber, and ϕ is an azimuthal coordinate. We defined the sea spectrum, W(K) as follows:

$$W(K) = \frac{S(K,\phi)}{K} \qquad (4.2)$$

For the VV case, a good approximation for the average radar backscattering coefficient is [Fung and Lee, 1983]

$$\sigma^o_{VV} = 8k^4|\alpha_{VV}|^2\, W(K) \qquad (4.3)$$

where:

k = radar wavenumber

K = 2sinθ = ocean wavenumber

θ = incident angle.

$$\alpha_{VV} = R_V\cos^2\theta + \left(\frac{\varepsilon_r - 1}{2\varepsilon_r}\right)(1 + R_V)^2 \sin^2\theta$$

$$R_V = \frac{\varepsilon_r\cos\theta - (\varepsilon_r - \sin^2\theta)^{1/2}}{\varepsilon_r\cos\theta + (\varepsilon_r - \sin^2\theta)^{1/2}}$$

ε_r = relative complex dielectric constant.

Thus calculation of the sea spectrum, W(K), was made using the equation

$$W(K) = \frac{\sigma^o_{VV}}{8k^4|\alpha_{VV}|^2} \qquad (4.4)$$

4.3 Comparison with Previous Measurements and with Model

The results obtained from this experiment can be compared with the semi-empirical model proposed by Fung and Lee, [1982]/ For comparison, this model predicts that, for the range of K shown in our figures, the value of W(K) is given by [Lawner and Moore, 1985]

$$W(K) = \frac{.875\ (2\pi)^{\rho-2}\left(1 + \frac{3K^2}{k_m^2}\right)\ g^{\left(\frac{1-\rho}{2}\right)}}{K\left[K\left(1 + \frac{K^2}{k_m^2}\right)\right]^{\left(\frac{\rho+1}{2}\right)}} \left[1 + 2\left(\frac{1-R}{1+R}\right)\right]$$

where:

$k_m^2 = \frac{g\rho}{\tau} = (3.73)^2\ cm^{-2}$

$g = 981\ cm/s^2$

ρ = sea water density

τ = sea surface tension

and R is the ratio of slope variances in the crosswind and upwind directions as given by Cox and Munk's [1954] clean sea model:

$$R = \frac{\sigma_{ct}^2}{\sigma_{ut}^2} = \frac{.003 + 1.92 \times 10^{-3}\ u_{12.5}}{3.16 \times 10^{-3}\ u_{12.5}}$$

and $u_{12.5}$ = wind speed at a height of 12.5 meters in meters per second.

The results shown in Figures 4.1 - 4.4 fall much closer to the semi-empirical model than earlier tower results made in 1979 from the Noordwijk tower [Lawner and Moore, 1985]. The earlier results could only be brought into good agreement with the model after compensating empirically for the difference between tower-based and air/spacecraft measurements. This seemed reasonable since the model was based on air/spacecraft measurements as opposed to tower-based measurements. However, the present results do not seem to need such an adjustment since they are already in fairly close agreement with the model. The reason for this that there is little bias between the tower-based and aircraft measurements at large incidence angles.

5.0 MEASUREMENTS OF THE MODULATION TRANSFER FUNCTION

Consider a microwave antenna illuminating a portion of the ocean surface small in comparison with the wavelength of any long ocean waves. The primary scatterers are short waves (ripples), a few centimeters in length, that are riding on the long ocean waves. Since the radar only detects the short waves,

the detectability of the long ocean waves by radar becomes possible by modulatng the radar return power by the long ocean waves.

For low to moderate sea states, the linear model introduced by Keller and Wright [1975] is used to describe the modulation. As shown in Figure 5.1, the proposed model assumes that the scattered power is linearly dependent on the long ocean wave through a transfer function R(f).

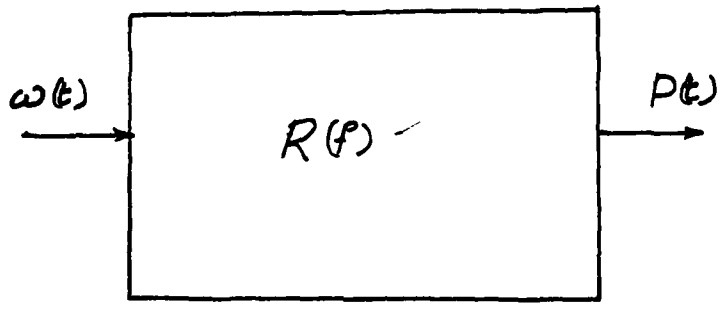

FIGURE 5.1: A Linear System

Using linear network theory, with the height of a long ocean wave represented by W(t) and radar return power by P(t), we find

$$R(f) = \frac{S_{W,P}}{S_{W,W}} \tag{5.1}$$

where $S_{W,W}$ is the spectrum of the waveheight and $S_{W,P}$ is the cross-spectrum of the wave height and power. Note that the above equation can be represented in the time domain by

$$P(t) = \overline{P} + RW(t) \tag{5.2}$$

where $\overline{P}$ is the mean scattered power.

Normalizing (5.1) by $\overline{P}$ and defining

$$m(f) = \frac{R(f)}{K},$$

the modulation transfer function m(f), as defined by Keller and Wright [1975] is obtained.

$$m(f) = \frac{S_{W,P}}{K\overline{P}S_{W,W}} \tag{5.3}$$

where K is the wave number of the long ocean waves at frequency f.

An important quantity in analysis of this type is the coherence function defined by

$$coh^2(f) = \frac{|S_{W,P}|^2}{|S_{P,P}| \cdot |S_{W,W}|}$$

If $S_{P,P}$ is proportional to $S_{W,W}$, the coherence function has a value of one at any given frequency. Values less than one indicate either (a) noisy signals, (b) nonlinearities, or (c) $S_{P,P}$ is due to sources in addition to $S_{W,W}$.

Two sources of modulation of the scattered microwave power exist. These are the tilt modulation and the hydrodynamic modulation. Therefore, the modulation transfer function can be broken down into two components:

$$R = R_{tilt} + R_{hydro} \tag{5.4}$$

5.1 Tilt Modulation

The tilt modulation is due to the fact that the ripples are seen by the radar at different local incidence angles depending on their location on the long waves. The backscatter from the ripples involves Bragg resonance with a ripple component of wavelength $\Lambda_B = \lambda/2 \sin\theta_L$, where λ is the radar wavelength and θ_L is the local angle of incidence.

The Bragg scattering cross-section per unit area for a tilted facet is given by

$$\sigma^o_{pp}(\theta_{L1}\psi) = 8K^4\sigma_1^4\cos^4\theta_L \ |\alpha_{pp}|^2 \ W_4(\theta_{L1}\psi) \tag{5.5}$$

Assuming that the short wave spectrum is a Phillips spectrum, (5.5) takes the form

$$\sigma^0 \propto \frac{\cos^4\theta_L}{K^4} = \frac{\cos^4\theta_L}{(2k\sin\theta_L)^4} \propto \cot^4\theta_L$$

where θ_L is the local angle of incidence. Denoting the long wave slopes by S and the pointing angle by θ_p, we have

$$\theta_L = \theta_p + \tan^{-1} S$$

Then

$$\sigma^0 \propto \left[\frac{1 + S\tan\theta_p}{\tan\theta_p - S} \right]^4 \tag{5.6}$$

The Taylor series expansion of the above expression results in

$$\sigma^0 \propto \frac{1}{\tan^4\theta_p} - \left[\frac{4}{\tan^5\theta_p} + \frac{4}{\tan^3\theta_p}\right] S + \left[\frac{10}{\tan^6\theta_p} + \frac{16}{\tan^4\theta_p} + \frac{6}{\tan^2\theta_p}\right] S^2$$

$$- \left[\frac{20}{\tan^7\theta_p} + \frac{40}{\tan^5\theta_p} + \frac{24}{\tan^3\theta_p} + \frac{4}{\tan\theta_p}\right] S^3 + \ldots$$

$$\equiv \alpha_0 + \alpha_1 S + \alpha_2 S^2 + \ldots \tag{5.7}$$

If only one ocean wave were present, we could write waveheights and slopes as

$$\begin{aligned} W(t) &= A\cos(kx + 2\pi f_o t) = A\cos\phi \\ S &= -AK\sin\phi \end{aligned} \tag{5.8}$$

Equation (5.7) can be simplified to

$$\sigma^0 \propto \bar{\sigma}^0 + \left[(AK)\alpha_1 + \frac{3\alpha_3}{4}(AK)^3 + \ldots\right] \sin\phi$$

$$- \left[\frac{\alpha_2}{2}(AK)^2 + \frac{\alpha_4}{2}(AK)^4 + \alpha_6 \frac{15}{32}(AK)^6 + \ldots\right] \cos^2\phi$$

$$- \left[\frac{\alpha_3}{4}(AK)^3 + \frac{5}{16}\alpha_5(AK)^5 + \ldots\right] \sin^3\phi + \ldots \quad (5.9)$$

Notice that harmonics of the ocean wave frequency are present in the scattered power and the amplitude of each harmonic is nonlinearly related to the ocean waveheight. A measure of first-order amplitude nonlinearity can be obtained by considering the ratio

$$r_1 = \frac{3/4\ \alpha_3(AK)^3}{(AK)\alpha_1} = \frac{3}{4}\frac{\alpha_3}{\alpha_1}(AK)^2 \quad (5.10)$$

Similarly, for the lowest-order harmonic nonlinearity we can define r_2 as

$$r_2 = -\frac{\alpha_2(AK)^2}{2AK\alpha_1} = -1/2\ (AK)\ (\alpha_2/\alpha_1) \quad (5.11)$$

The ratios r_1 and r_2 at different pointing angles and for slopes of 0.1 and 0.3 are given in Table 4. As seen, at specific pointing angles and for steep slopes of the long waves, the process is nonlinear. One consequence of the nonlinearities is that the amplitude of the tilt modulation transfer function decreases as the slope increases.

TABLE 4

RATIOS r_1 AND r_2 AT DIFFERENT SLOPES AND POINTING ANGLES

θ_p	r_1(AK=0.1)	r_1(AK=0.3)	r_2(AK=0.1)	r_2(AK=0.3)
20	0.320	2.880	0.371	1.110
30	0.152	1.371	0.259	0.777
40	0.096	0.864	0.212	0.636
50	0.075	0.675	0.194	0.582
60	0.071	0.639	0.202	0.606
70	0.100	0.901	0.251	0.753

To illustrate the effects of the nonlinearities, we assume that only the

first three terms of (5.7) are significant. Then we have

$$P(t) \propto \alpha_o + \alpha_1 S + \alpha_2 S^2$$

Assuming that slopes are normally distributed, it is shown in Appendix 1 that the spectrum of the received power is given by:

$$S_{pp}(\omega) \propto C'\delta(\omega) + \alpha_1^2 \omega^2 S_{W,W} + \frac{1}{\pi}(\alpha_1\alpha_2 + \alpha_2^2)\left[(\omega^2 S_{W,W}) * (\omega^2 S_{W,W})\right]$$

Also in Appendix 1, the cross-spectrum of wave height and power has been derived as

$$S_{W,P}(\omega) \simeq \alpha_1 \omega^2 S_{W,W} + \alpha_2\left(\frac{1}{2\pi}\right)\left[(\omega^2 S_{W,W}) * (\omega^2 S_{W,W})\right]$$

where * denotes convolution.

Then, from (5.3) we have

$$m(f) \propto \frac{\alpha_1}{K\overline{P}} + \frac{\alpha_2(1/2\pi)\left[(\omega^2 S_{W,W}) * (\omega^2 S_{W,W})\right]}{\omega^2 K\overline{P} S_{W,W}}$$

Notice that the second term of the above equation is due to the effects of the nonlinearities.

5.2 Hydrodynamic Modulation

If one assumed that the ripple amplitudes were uniform over a large-scale wave, the modulation of the received signal would be completely governed by the tilt modulation. Hydrodynamic modulation of the ripples causes a non-uniform distribution of the ripples over the long ocean waves.

If the spectrum of the short waves S(K) and the slopes of the long waves are known, the scattering coefficient due to the tilt effect can be computed as follows:

$$\sigma^o_{VV}(t) = \frac{2k^3}{\pi \sin\theta_L}\left|R_V \cos^2\theta_L + 1/2(1 - \frac{1}{\epsilon})(1 + R_V)^2 \sin^2\theta_L\right|^2 S(\delta k \sin\theta_L) \qquad (5.12)$$

where:

$$\theta_L = \theta_p + \tan^{-1} S$$

R_V = Fresnel reflection coefficient

ε = dielectric constant of the sea

$S(\cdot)$ = sea spectrum

The tilt modulation can be removed from the scattering coefficient to obtain

$$\Delta\sigma^o(t) = \sigma^o_m(t) - \sigma^o_{th}(t) \tag{5.13a}$$

$$\sigma^o_{th}(t) \triangleq \frac{\overline{\sigma^o_m(t)}}{\overline{\sigma^o_{VV}(t)}}\,\sigma^o_{VV}(t) \tag{5.13b}$$

where $\sigma^o_m(t)$ is the measured backscattering coefficient, and $\sigma^o_{VV}(t)$ is given in (5.12). Normalization shown in (5.13b) is necessary because the absolute level of the theoretical σ^o used for tilt modulation may not agree with experiment. A hydrodynamic modulation transfer function can then be calculated by using the modified scattering coefficient, instead of the actual scattering coefficient, in the MTF calculations.

5.3 Calculation of the MTF

Equation (5.1) is used to calculate the MTFs. The spectral quantities in (5.1) must be replaced by the weighted sum of their periodograms, obtaining the following equation:

$$m(f) = \frac{\overline{|P(f)W^*(f)|}}{\overline{p}\,\frac{\omega^2}{g}\,\overline{|W(f)|^2}} \tag{5.14}$$

where the overbar denotes ensemble averaging. Accordingly, the coherence function can be calculated as

$$\mathrm{coh}^2(f) = \frac{\overline{|P(f)W^*(f)|^2}}{\overline{|P(f)|^2}\;\overline{|W(f)|^2}} \tag{5.15}$$

In order for the periodograms in the above equation to be good estimates of the power spectral density, averaging over many subsets of a long data set is required. This, in turn, requires that the environmental conditions over the whole period of the run be reasonably stable. Unfortunately, this has not

been the case for the Nordsee data. Figure 5.2 shows the wave height spectra of two seven-minute periods separated by a ten-minute interval. Comparing the two power spectra, notice that the waveheight spectrum in the second graph has shifted to the right. This shift in the dominant waveheight frequency does not allow averaging over the entire period to obtain more degrees of freedom. Considering these problems, the long runs were divided into subsets of 100 seconds each to calculate the spectra. Each subset was padded with zeros to make a 128-second subset. The Fourier transform of each subset was multiplied by a moving average window function. After multiplying by the window function, seven 128-second runs were averaged to compute the associated power density spectra.

With the environmental conditions changing rapidly, it was necessary to shorten the run time. However, use of the shortened time span to accommodate the rapidly changing environmental conditions caused the spectra to have large variances.

To increase the accuracy of the spectra, a more advanced method of spectral estimation is needed. The Singular Value Decomposition (SVD) method introduced by Cadzow [1982] is probably the most suitable method. A program currently under development at the Remote Sensing Laboratory of the University of Kansas employs this method to compute the power spectral densities and MTFs. Upon completion of the testing of the testing of this program, it will be used in computing the MTFs.

5.4 Preliminary Results

Figure 5.3 shows a sample run in the upwind direction at a radar frequency of 10 GHz and a wind speed of 18.8 m/s. The spectrum of the wave height shows a single peak at a frequency of 0.15 Hz.

The magnitude and phase of the MTF are plotted in Figures 5.3b and 5.3c, respectively. The phase of the MTF is close to zero at the point of high coherency and the MTF has a magnitude of about 0.8 at that frequency. The low values of the MTF clearly illustrate that at high wind speeds (high slopes) the assumed linear relationship is weak and the process could be better described by a nonlinear model.

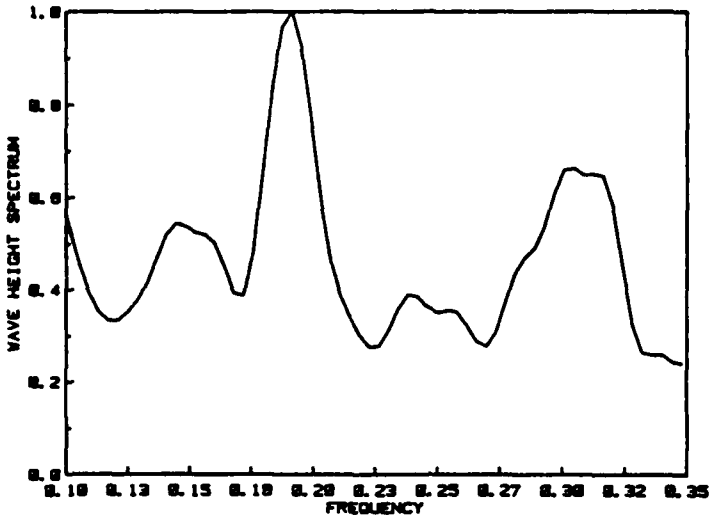

a

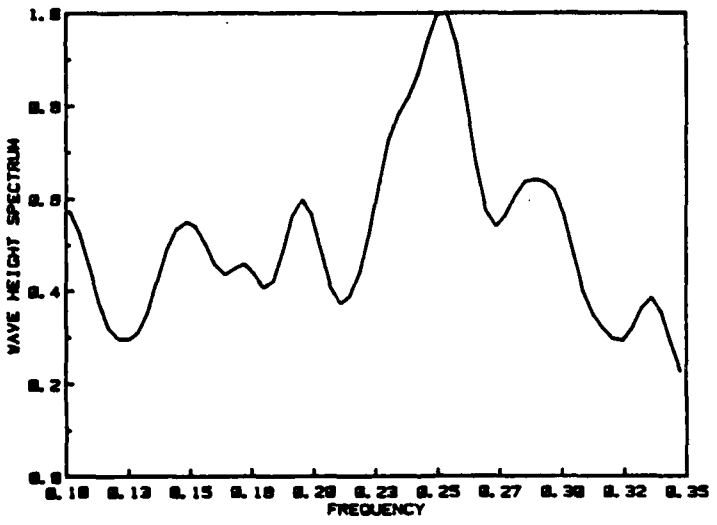

b

FIGURE 5.2: Spectra of Waveheight Calculated from Vertically Polarized 5.3 GHz Backscatter at a Pointing Angle of 55° and at a Wind Speed of 8.8 m/s in the Upwind Direction.

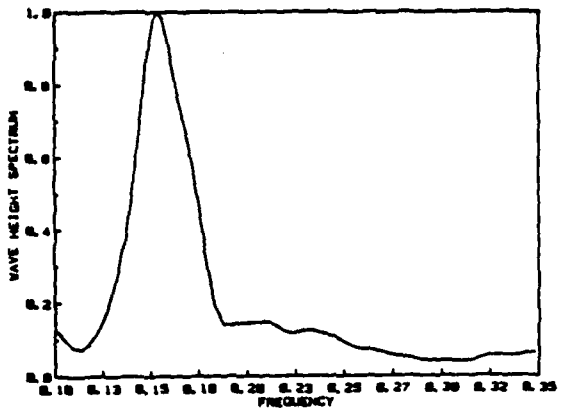

a

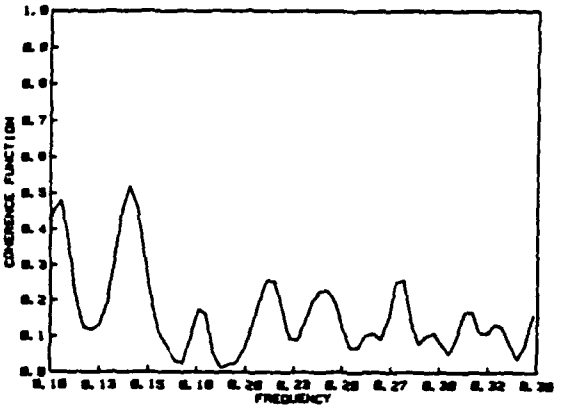

d

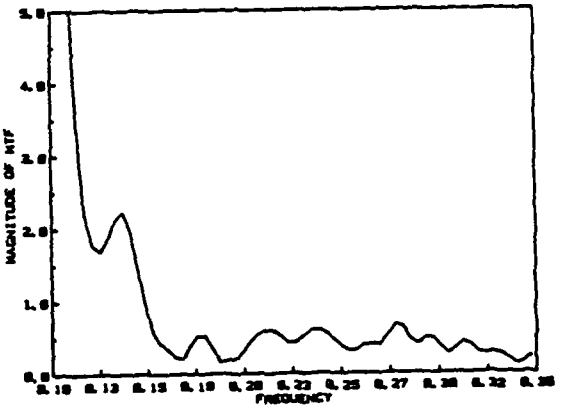

b

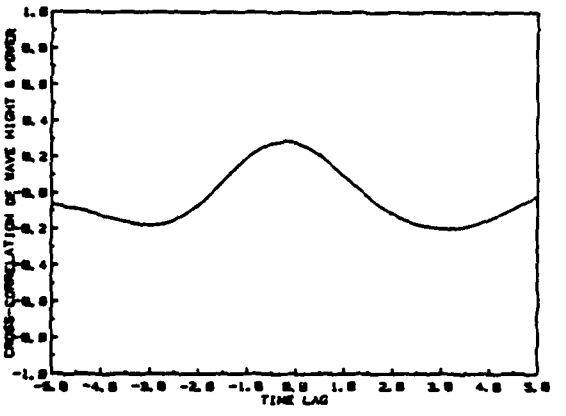

e

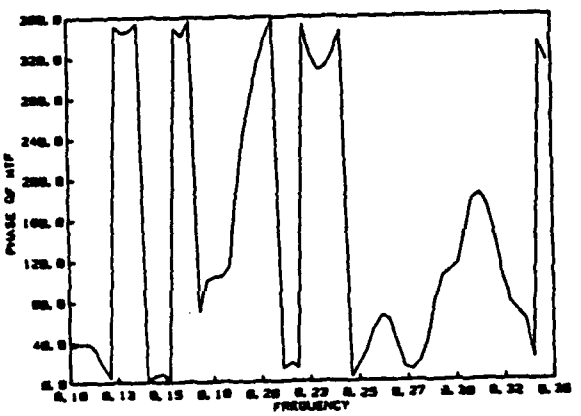

c

FIGURE 5.3: Sample Run for a Vertically Polarized 10 GHz Backscatter at a Pointing Angle of 64.8° and at a Wind Speed of 18.8 m/s in the Upwind Direction.

One method of improving the calculation is to calculate the MTFs using the $\Delta\sigma^0$, as explained in the previous sections. The result is shown in Figure 5.4. Notice that the magnitude of MTF has increased. This demonstrates the fact that removing the tilt modulation to some extent has linearized the process. The higher values of coherence function and cross-correlation in Figure 5.4 agree with this conclusion. Since the MTF in Figure 5.4 is the hydrodynamic portion of the modulation transfer function, one could argue that the hydrodynamic modulation is more linear than the tilt modulation at high wind speeds.

Figure 5.5 shows the spectrum of the waveheight, MTF, phase of the MTF, coherence function and the cross-correlation function for vertically polarized 15 GHz backscatter at a wind speed of 16.5 m/s in the upwind direction. The magnitude of the MTF is approximately equal to the magnitude of the MTF for the 10 GHz case, but the phase is close to 320° in this case.

Figure 5.6 shows the plots of hydrodynamic modulation transfer function and the cross-correlation of $\Delta\sigma^0$ and waveheight. Notice that the MTF has decreased compared to the previous case while its phase has essentially remained unchanged.

In conclusion, we emphasize that, since the microwave power is nonlinearly related to the ocean wave height, the concept of the MTF is not applicable for higher waves and slopes. A nonlinear model is needed to describe the relationship between the scattered power and the ocean wave height.

6.0 CONCLUSIONS

This paper extends the results presented earlier to include the sea spectrum computed from the scattering coefficients and the modulation transfer function computed from the selected data. In addition, problems associated with the computation of the modulation transfer functions are discussed. The scattering coefficients presented are accurate up to ± 1 dB and no systematic calibration errors have been observed.

It was not possible to make comparisons with the aircraft data because they are not presently available to The University of Kansas. A detailed data analysis will have to await receipt of results from the other investigators.

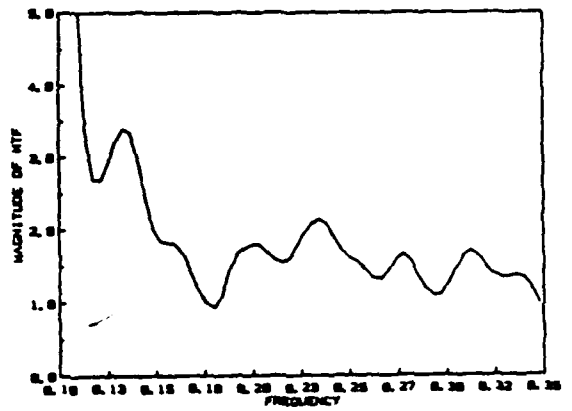

a

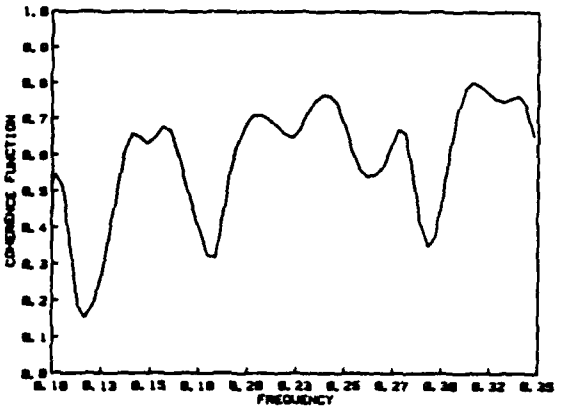

c

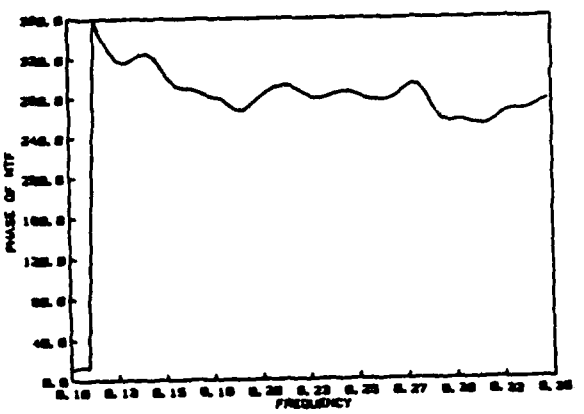

b

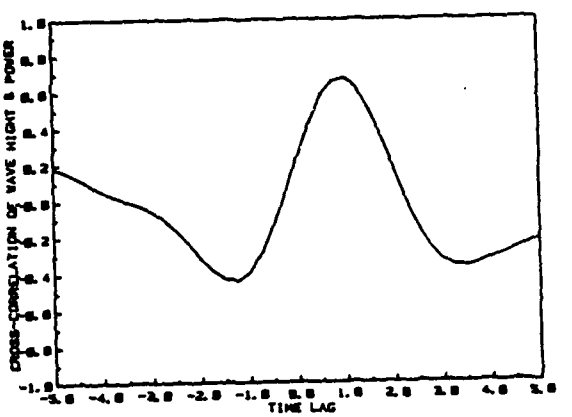

d

FIGURE 5.4: Sample Run for a Vertically Polarized 10 GHz Backscatter at a Pointing Angle of 64.8° and at a Wind Speed of 18.8 m/s in the Upwind Direction.

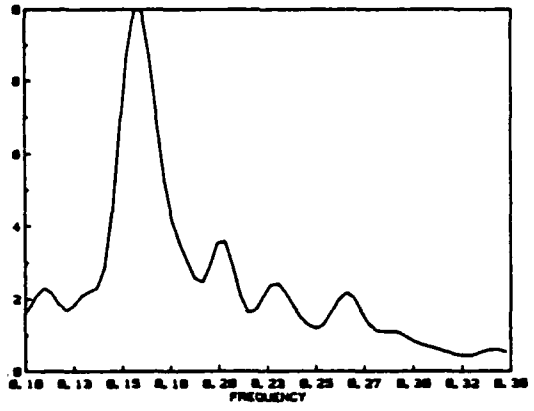

a

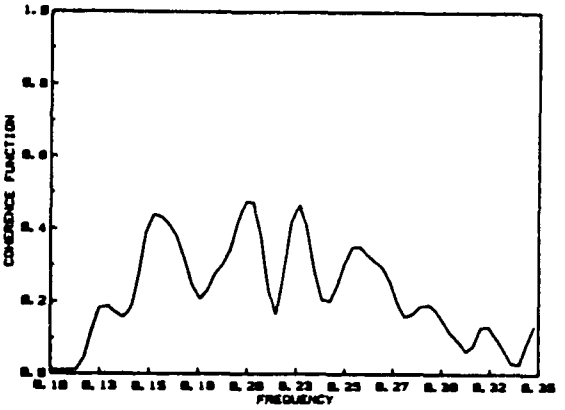

d

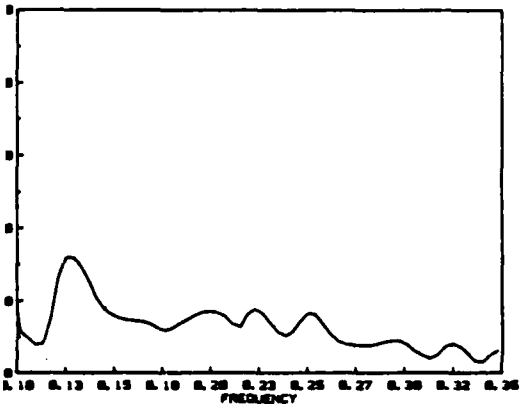

b

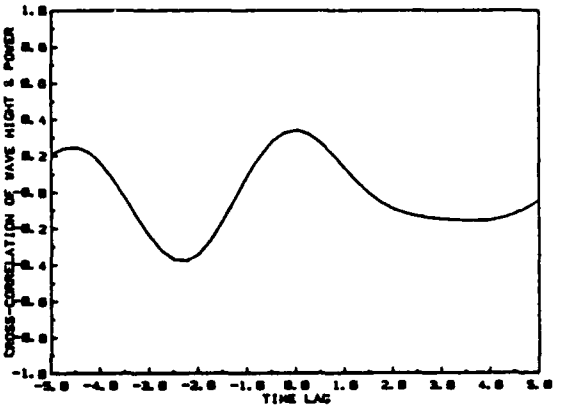

e

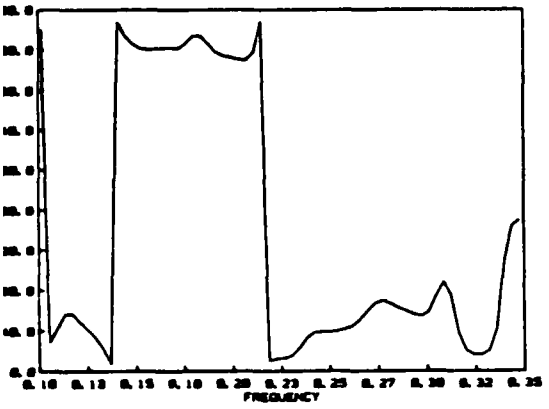

c

FIGURE 5.5: Sample Run for a Vertically Polarized 15 GHz Backscatter at a Pointing Angle of 55° and at a Wind Speed of 16.5 m/s in the Upwind Direction.

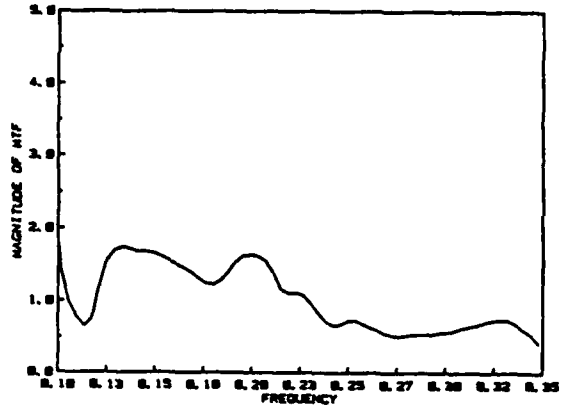

a

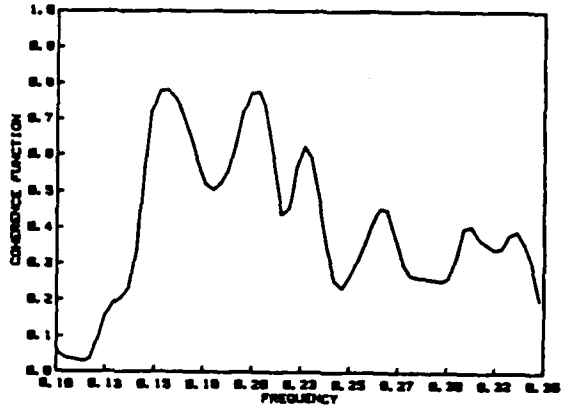

c

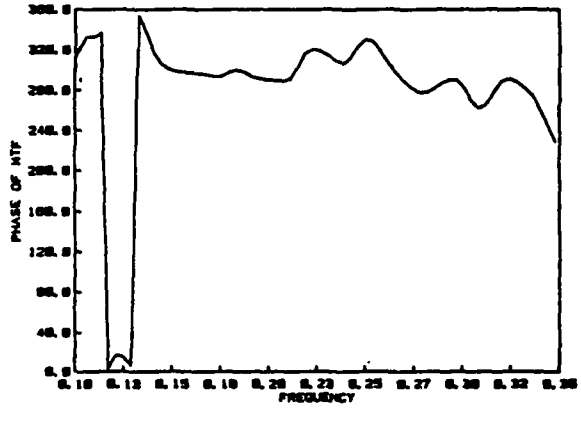

b

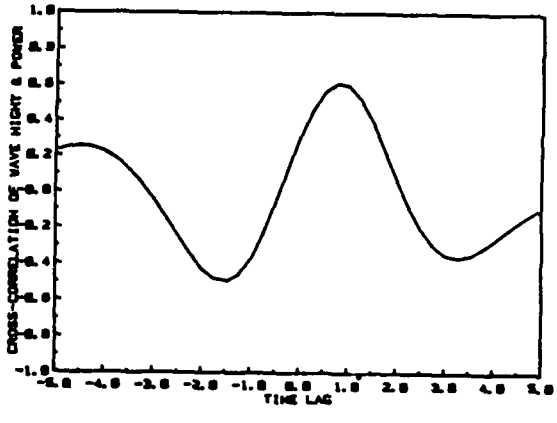

d

FIGURE 5.6: Sample Run for a Vertically Polarized 15 GHz Backscatter at a Pointing Angle of 55° and at a Wind Speed of 16.5 m/s in the Upwind Direction.

REFERENCES

Cadzow, J.A., "Spectral Estimation: An Overdetermined Rational Model Equation Approach," Proc. IEEE, vol. 70, no. 9, pp. 907-939, September 1982.

Claassen, J.P., et al., "Radar Sea Return and the RADSCAT Anemometer," Proceedings of OCEANS'72 IEE Int'l. Conference Record, pp. 180-185, September 1972.

Cox, C. and W. Munk, "Statistics of the Sea Surface Derived from Sun Glitter," J. Marine Res., vol. 13, pp. 198-227, 1954.

Daley, J.C., "Wind Dependence of Radar Sea Return," J. Geophys. Res., vol. 78, pp. 7823-7833, 1973.

Fung, A.K. and H.L. Chan, "A Theory of Sea Scatter at Large Incident Angles," J. Geophys. Res., vol. 82, pp. 3439-3444, 1977.

Fung, A.K. and K.K. Lee, "A Semi-Empirical Sea-Spectrum Model for Scattering Coefficient Estimation," IEEE J. Oceanic Engr., vol. OE-7, no. 4, pp. 166-176, October 1982.

Fung, A.K. and K.K. Lee, "Variation of Sea Wave Spectrum with Wind Speed," Digest of IGARSS'83, vol. 2, San Francisco, California, August 31 - September 2, 1983. (IEEE Catalog No. 83CH1837-4).

Gogineni, S., et al., "Mobile Microwave Spectrometer Measures Radar Backscatter," Microwaves & RF, vol. 23, no. 9, pp. 156-166, September 1984.

Jones, W.L., et al., "Aircraft Measurements of the Microwave Scattering Signature of the Ocean," IEEE Trans. Ant. Prop., vol. AP-25, pp. 52-61, 1977.

Keller, W.C. and J.W. Wright, "Microwave Scattering and the Straining of Wind-Generated Waves," Radio Science, vol. 10, no. 2, pp. 139-147, February 1975.

Lawner, R.T. and R.K. Moore, "Short-Gravity and Capillary Wave Spectra from Tower-Based Radar," to be published in IEEE J. Oceanic Engr., Special Issue, January 1985.

Moore, R.K. and W.J. Pierson, Jr., "Worldwide Oceanic Wind and Wave Predictions Using a Satellite Radar Radiometer," J. Hydronautics, vol. 5, no. 2, pp.52-60, April 1971.

APPENDIX 1
DERIVATION OF THE RADAR SIGNAL SPECTRA

Assume that $P(t) \propto \alpha_0 + \alpha_1 S + \alpha_2 S^2$. Then

$$R_{pp}(\tau) \propto E\{[\alpha_0 + \alpha_1 S(t) + \alpha_2 S^2(t)][\alpha_0 + \alpha_1 S(t+\tau) + \alpha_2 S^2)t+\tau)]\}$$

$$= \alpha_0^2 + E\{S(t)S(t+\tau)\}\ \alpha_1^2 + \alpha_0\alpha_1 E[S(t+\tau)]$$

$$+ \alpha_0\alpha_2 E[S^2(t+\tau)] + \alpha_0\alpha_1 E[S(t)] + \alpha_1\alpha_2 E[S(t)\ S^2(t+\tau)]$$

$$+ \alpha_0\alpha_2 E[S^2(t)] + \alpha_1\alpha_2 E[S^2(t)\ S(t+\tau)] + \alpha_2^2 E[S^2(t)S^2(t+\tau)]$$

Assume that the slopes are normally distributed with mean equal to zero. Let

$$S(t) = S \text{ and } Y = S(t+\tau)$$

Then

$$E[S(t)\ S^2(t+\tau)] = E[SY^2]$$

$$E[SY^2] = E[S \cdot E\{Y^2|S\}] = E\{S[\sigma_2^2\ (1-r^2) + \frac{r^2\sigma_2^2}{\sigma_1^2} X^2]\}$$

where $\sigma_1^2 = E(S^2)$ and $\sigma_2^2 = E(Y^2)$ and r is the correlation coefficient. Thus,

$$E(SY^2) = \frac{r^2\sigma_2^2}{\sigma_1^2} E(S^3) = \frac{r^2\sigma_2^2}{\sigma_1^2} \sigma_1^4 = r^2\sigma_1^2\sigma_2^2 = E^2[YS]$$

Therefore,

$$E[S(t)\ S^2(t+\tau)] = E^2[S(t)\ S(t+\tau)] = R_{SS}^2\ (\tau)$$

The autocorrelation of the power can be simplified to

$$R_{pp}(\tau) \propto C + \alpha_1^2 R_{SS}(\tau) + 2\alpha_1\alpha_2 R_{SS}^2(\tau) + 2\alpha_2^2 R_{SS}^2(\tau)$$

Defining

$$S_{pp}(\omega) = FT\{R_{pp}(\tau)\}$$

We have,

$$S_{pp}(\omega) \propto C' \delta(\omega) + \frac{1}{\pi}[S_{S,S}(\omega) * S_{S,S}(\omega)](\alpha_1\alpha_2 + \alpha_2^2) + \alpha_1^2 S_{S,S}(\omega)$$

Similarly, the cross-spectrum of power and slope could be found

$$S_{P,S} \propto FT\{R_{P,S}\} = FT\{\alpha_1 R_{SS}(\tau) + \alpha_2 E[S(t)S^2(t+\tau)]\}$$

$$= FT\{\alpha_1 R_{SS}(\tau) + \alpha_2 R_{SS}^2(\tau)\} = \alpha_1 S_{SS} + \alpha_2(\frac{1}{2\pi}) S_{S,S} * S_{S,S}$$

CRINC LABORATORIES

Chemical Engineering Low Temperature Laboratory

Remote Sensing Laboratory

Flight Research Laboratory

Chemical Engineering Heat Transfer Laboratory

Nuclear Engineering Laboratory

Environmental Health Engineering Laboratory

Information Processing Laboratory

Water Resources Institute

Technical Transfer Laboratory

Air Pollution Laboratory

Satellite Applications Laboratory

END

FILMED

4-85

DTIC